MATERIALS SCIENCE

Out-of-plane ferroelectricity and robust magnetoelectricity in quasi-two-dimensional materials

Xue-Zeng Lu[1], Hui-Min Zhang[1], Ying Zhou[1], Tong Zhu[2], Hongjun Xiang[3,4], Shuai Dong[1], Hiroshi Kageyama[2], James M. Rondinelli[5]*

Thin-film ferroelectrics have been pursued for capacitive and nonvolatile memory devices. They rely on polarizations that are oriented in an out-of-plane direction to facilitate integration and addressability with complementary metal-oxide semiconductor architectures. The internal depolarization field, however, formed by surface charges can suppress the out-of-plane polarization in ultrathin ferroelectric films that could otherwise exhibit lower coercive fields and operate with lower power. Here, we unveil stabilization of a polar longitudinal optical (LO) mode in the n = 2 Ruddlesden–Popper family that produces out-of-plane ferroelectricity, persists under open-circuit boundary conditions, and is distinct from hyperferroelectricity. Our first-principles calculations show the stabilization of the LO mode is ubiquitous in chalcogenides and halides and relies on anharmonic trilinear mode coupling. We further show that the out-of-plane ferroelectricity can be predicted with a crystallographic tolerance factor, and we use these insights to design a room-temperature multiferroic with strong magnetoelectric coupling suitable for magneto-electric spin-orbit transistors.

INTRODUCTION

Ferroelectrics have been intensively studied since the discovery of $BaTiO_3$ and are of modern interest because of their ability to achieve bistable electrical polarizations that can be used in nonvolatile memory devices (*1*–*5*). Recently, Hf-based ferroelectrics have demonstrated a path to achieve complementary metal-oxide semiconductor (CMOS)–compatible ferroelectric integration; however, they suffer from a variety of limitations, including sizable leakage, and large coercivity, especially in ultrathin films that lead to poor energy efficiencies (*6*–*11*). For device integration and miniaturization, the ferroelectric polarization should be oriented in the out-of-plane direction, i.e., along the film-growth direction, and persist as the film thickness decreases. The former requirement can be realized more often in perovskite oxides, but it is much more challenging to realize in layered (quasi-)two-dimensional compounds, e.g., in Ruddlesden-Popper (RP) structures (*12*–*15*), with a rock-salt layer interrupting the perovskite layers, which imposes a coherence length constraint on the polar distortion (*16*), and to achieve strong polar mode-strain coupling to reorient the bulk in-plane polarization to an out-of-plane direction in thin films. In cases where the out-of-plane polarization naturally occurs or is engineered, the second requirement can be challenging to satisfy as the polarization in the thin film can be suppressed by the depolarizing field formed by surface charges. As a result, there is frequently an unavoidable critical thickness for most ferroelectrics below which the out-of-plane polarization vanishes (*17*, *18*), rendering them nonfunctional for device applications.

There are two unique ferroelectric materials classes distinct from conventional proper soft-mode and second-order Jahn-Teller active systems that can exhibit electric polarizations under open-circuit boundary conditions: hyperferroelectrics (*19*) and geometric improper ferroelectrics (*19*, *20*). In contrast to the rarer hyperferroelectrics class (*19*, *21*–*24*), a subset of improper ferroelectrics (*12*, *25*–*29*), so-called hybrid improper ferroelectrics, circumvent depolarizing field effects owing to their geometric rather than electrostatic origins for an electric polarization. The known available materials exclusively exhibit in-plane ferroelectricity, however, transverse to the desired normal direction of the film. Nonetheless, they can be readily predicted by lowering the tolerance factor through changes in chemistry to favor rotations of metal-oxygen octahedra. Although the ferroelectric (FE) mode is stable, its condensation is induced by mode-mode coupling among the FE mode and other nonpolar phonon modes, such as octahedral rotational modes. These RP-structured materials have a range of functional properties derived from the form of the trilinear interaction coupling the modes, including the switching of weak ferromagnetism (wFM) with an electric field in $Ca_3Mn_2O_7$ (*27*) and a low coercive field for the switchable polarization and abundant charged FE domain walls in $(Ca,Sr)_3Ti_2O_7$ single crystals (*30*), leading to topological vortices and antivortices (*31*). Nonetheless, the polar ground-state structure always exhibits $Cmc2_1$ symmetry with an in-plane polarization, although an electric-field stabilized $Pna2_1$ phase with out-of-plane polarization was observed in experiment in nonmagnetic $Li_2Sr_{1-x}Ca_xNb_2O_7$ (*32*). To make these RP materials competitive alternatives for microelectronic integration, a polar phase with persistent out-of-plane ferroelectricity is required. Furthermore, controllable wFM still has not been observed in RP (*33*, *34*) or Dion-Jacobson phases (*35*, *36*), which may be because the controllable wFM through the out-of-plane rotation and in-plane tilt (e.g., X_2^+ and X_3^- in RP phases, respectively) requires different magnetic structures. In addition, selectivity of the octahedral rotation mode involved in the polarization switching path is not easy to achieve. Therefore, a deterministic and intrinsic constraint on the

[1]Key Laboratory of Quantum Materials and Devices of Ministry of Education, School of Physics, Southeast University, Nanjing 211189, People's Republic of China. [2]Graduate School of Engineering, Kyoto University, Nishikyo-ku, Kyoto 615-8510, Japan. [3]Key Laboratory of Computational Physical Sciences (Ministry of Education), Institute of Computational Physical Sciences, and Department of Physics, Fudan University, Shanghai 200433, People's Republic of China. [4]Shanghai Qi Zhi Institute, Shanghai 200030, People's Republic of China. [5]Department of Materials Science and Engineering, Northwestern University, Evanston, IL 60208, USA.
*Corresponding author. Email: jrondinelli@northwestern.edu

polarization switching is desirable. To realize this constraint, there should be a single magnetic structure that allows either rotation mode to be active in the polarization reversal, avoiding the need for selectivity and kinetic control in the switching process.

Here, by using first-principles calculations, we unveil a general polar longitudinal optical (LO) mode, which both produces out-of-plane ferroelectricity and persists under open-circuit boundary condition in $n = 2$ RP halides and sulfides. This previously unidentified polar mode comprises cation and anion displacements in the rock-salt layers and transforms as the irreducible representation (irrep) Γ_3^-. We find that $KAg_2Mn_2Cl_7$, $SrTb_2Fe_2S_7$, and $BaLa_2In_2S_7$ exhibit hybrid improper ferroelectricity (HIF) and trilinear interactions stabilize the Γ_3^- mode with calculated electric polarizations ranging from 0.012 to 4.03 μC cm^{-2} in films of unit cell thicknesses. We further show with constrained electric displacement field calculations and in a slab structure (e.g., 2.3-nm thin film) of $KAg_2Mn_2Cl_7$ that the polarizations persist under open-circuit boundary conditions. Furthermore, $KAg_2Mn_2Cl_7$ and $SrTb_2Fe_2S_7$ are magnetoelectric (ME) multiferroics with strong coupling between the out-of-plane polarization and magnetization. The Néel temperature for $KAg_2Mn_2Cl_7$ and $SrTb_2Fe_2S_7$ can be as high as 50 and 800 K, respectively, and their FE Curie temperatures are 274 and 455 K, respectively. Last, we show that the appearance of the Γ_3^- mode in the halides and sulfides can be understood with the perovskite tolerance factor; low tolerance factors favor a polar phase with the polar LO displacements, which makes it a useful descriptor to find additional ferroic materials. Our work provides a general strategy to design strong ME coupling with out-of-plane hybrid improper ferroelectricity for integration into future microelectronic devices.

RESULTS

$K_3Mn_2Cl_7$ has been synthesized and exhibits both HIF and G-type antiferromagnetic spin orders in the vicinity of ~64 K (*37*). With this as our prototype material, we substitute K ions in the rock salt layers with Ag while maintaining K in the perovskite layers to create $KAg_2Mn_2Cl_7$ (Fig. 1). This *A*-site ordering can produce an orthorhombic $Cmc2_1$ polar phase with an in-plane polarization if the tolerance factor remains sufficiently low (*14*, *30*, *33*, *37*). After we perform our genetic algorithm structural search (*38*, *39*), however, we uncover three polymorphs with lower energies: *P*1, $Pna2_1$, and *Pc*. We use these structures and a few additional candidate polymorphs to determine the ground state. As shown in Fig. 2A, the *Pc* structure is lowest in energy in our density functional theory (DFT) calculations at the Perdew-Becke-Erzenhof functional for solids (PBEsol) (2 meV/f.u. lower than $Pna2_1$) and local density approximation (LDA) (11 meV/f.u. lower than $Pna2_1$) levels and it is dynamically stable (fig. S1). The greater stability of the *Pc* phase, obtained by using LDA rather than PBEsol, is because the *Pc* phase can accommodate the decrease of the cell volume better than the others through its stronger ability to host oxygen octahedral rotations (table S2). Full structural details are provided in table S3. Even with disorder on the *A* site, a *Pc*-like phase remains most stable. Thus, a weak *A*-site distribution disorder will still favor out-of-plane ferroelectricity in the halides (fig. S3).

The monoclinic *Pc* phase (tolerance factor $\tau = 0.944$) exhibits an electric polarization with both out-of-plane and in-plane components. The polarization vector in a Cartesian coordinate system [i.e., pseudo-tetragonal (pt) system] is given by $\mathbf{P} = (0.77, 0.77, 4.03)$ μC cm^{-2} with 97% percent of the polarization out-of-plane. The out-of-plane and in-plane polarizations arise from modes transforming as Γ_3^- and Γ_5^- (Fig. 1). Figure 2B shows that the Γ_3^- mode is a hard mode with respect to the *I*4/*mmm* phase and therefore cannot condense alone; furthermore, the in-plane polarization Γ_5^- only makes a minor contribution to the energy lowering. Our group theoretical analysis shows that there are three trilinear terms coupling these modes to other inversion-symmetry preserving displacements: $Q_{(\Gamma_3^-)}Q_{(M_5^+)}Q_{(M_5^-)}$, $Q_{(\Gamma_3^-)}Q_{(X_2^+)}Q_{(X_1^-)}$, and $Q_{(\Gamma_5^-)}Q_{(X_2^+)}Q_{(X_3^-)}$. Although the X_2^+ mode is a rotational mode, and has been found in previous studies to stabilize the in-plane polarizations in HIF (*12*, *14*, *27*, *30*, *40*, *41*), here, we find that X_2^+ is two dimensional with order parameter direction (*a*, *b*) and cannot be described as an effective one-dimensional order parameter as it is in polar RP phases with $Cmc2_1$ symmetry, i.e., (*a*, 0). It is essential to both the in-plane and out-of-plane polarizations. M_5^+ and M_5^- describe two antiferroelectric (AFE) modes and X_1^- is an octahedral rotational mode (Fig. 1). Therefore, the Γ_3^- mode also produces hybrid improper ferroelectricity and is induced by the two AFE modes and two rotational modes. Similarly, the latter trilinear interaction leads to condensation of the Γ_5^- mode and in this case, the displacements are to the chloride octahedra, i.e., tilting X_3^- and rotations X_2^+.

By using a phenomenological Landau model $F(u, \mathscr{E}) = E(u) - \Omega(u)\left[P(u)\mathscr{E} + \frac{1}{2}\varepsilon_0\chi_\infty(u)\mathscr{E}^2\right]$, the persistent polarization $P = -\frac{1}{\Omega}\frac{\partial F}{\partial \mathscr{E}} = \varepsilon_0\chi_\infty(u)\mathscr{E} + P(u)$ can be obtained when the electric displacement field $D = \varepsilon_0\mathscr{E} + P$ is zero (*19*, *21*). This nonzero polarization is highly sought, because it does not vanish in very thin films where the depolarizing field ($\mathscr{E}_d$) is very strong. Here u is the dimensionless order parameter for the polar mode in the *Pc* phase, i.e., $u = 1$ in the ground state. In our calculations, u is fixed at each value between 0 and 1.1, and the other internal degrees of freedom, amplitudes of the other phonon modes, and lattice parameters are relaxed. $\mathscr{E}$, Ω, *P*, ε_0, and χ_∞ are the depolarizing field, volume per formula unit, polarization, dielectric constant of free space, and the diagonal component of the high-frequency dielectric permittivity along the polarization direction, respectively. Because of the existence of the trilinear coupling interactions, the polynomial expansion of $E(u)$ can be equal to $\alpha u + \beta u^2 + \ldots$ in our calculations (fig. S4). Last, $\chi_\infty(u) = \varepsilon_\infty - 1$, where ε_∞ is the electronic contribution to the dielectric constant, and we find that it is nearly the same for the out-of-plane ($\varepsilon_\infty = 3.67$) and in-plane directions ($\varepsilon_\infty = 3.66$). We linearize $P(u) = P_s u$ as in previous studies (*19*, *21*), where P_s is the computed spontaneous polarization in the *Pc* phase. We thus obtain (0.17, 0.17, 0.76) μC cm^{-2} as the persistent polarization, which is comparable to that computed in the hexagonal FE *ABC* semiconductors (*19*). Our calculations with a slab model further show a remnant polarization under open-circuit boundary conditions (fig. S5), which is useful for achieving ultrathin film ferroelectricity (*42*). The out-of-plane polarization is comparable to that reported for $YMnO_3$ slab calculations (*20*), which is the prototype improper FE with a persistent polarization, exotic ME coupling, and vortex/antivortex domain structure (*20*, *28*, *43*, *44*), and is further

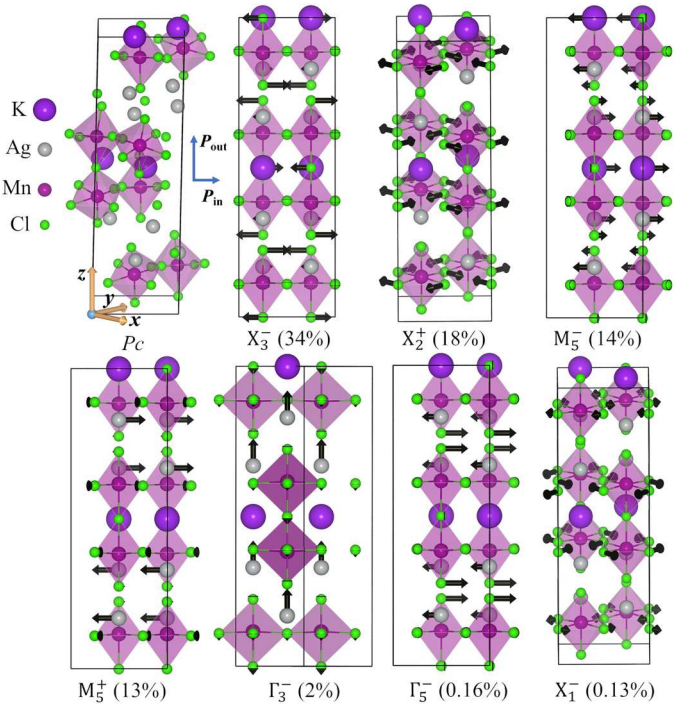

Fig. 1. Atomic structure of $KAg_2Mn_2Cl_7$. Ground-state structure of *Pc* $KAg_2Mn_2Cl_7$ and the main displacements, transforming as the designated irreps of the *I*4/*mmm* phase, contributing to its structure. Mode contributions (in percent) are given in descending order (as specified in parentheses). The pseudotetragonal Cartesian system and directions of the electric polarization ($\boldsymbol{P}_{out}$, out-of-plane polarization; $\boldsymbol{P}_{in}$, in-plane polarization) are also shown.

enhanced owing to surface polarization charges. Unlike $YMnO_3$, the out-of-plane persistent polarization occurs in $KAg_2Mn_2Cl_7$ from a trilinear coupling interaction with a positive LO mode yet will also lead to unambiguously strong ME coupling. Furthermore, the polar LO mode contributes 80% of the total out-of-plane polar distortion in the *Pc* structure, which is larger than those contributions found in the hexagonal *ABC* FEs (25 to 75%). The remnant polarization at $\boldsymbol{D} = 0$ takes 19% of the polarization at $\boldsymbol{E} = 0$ in $KAg_2Mn_2Cl_7$, which is much larger than those in the hexagonal *ABC* FEs (2 to 3.7%) (*19*), and may be attributed to the large portion of the LO mode and its lower frequency than the transverse optical (TO) mode in the out-of-plane polarization. Therefore, the RP phases may be a promising family for finding large remnant polarization at $\boldsymbol{D} = 0$. We find that the LO-TO splitting is usually smaller in improper FE RP materials than other materials (table S4). Unexpectedly, the polar LO mode in some RP improper FEs has a lower frequency than the polar TO mode, such as in $KAg_2Mn_2Cl_7$.

We find that $KAg_2Mn_2Cl_7$ exhibits the same G-type spin orders as $K_3Mn_2Cl_7$ with spins aligned along the long *c* axis of the crystal. wFM occurs, order 10^{-3} μB/Mn, which is comparable to that calculated for $K_3Mn_2Cl_7$ and measurable in experiment (*37*). It is oriented along the $[\bar{1}10]$ direction, such that it is in-plane and perpendicular to the in-plane component of the electric polarization (Fig. 2C). We use our computed Mn spin exchange parameters, $J_1 = 2.64$ meV and $J_2 = 3.16$ meV (in plane) and $J_3 = 2.25$ meV (out of plane), in our Monte Carlo simulations to obtain a Néel temperature of 50 K that is comparable to that in $K_3Mn_2Cl_7$ (Fig. 2D). A computed FE Curie temperature of 274 K in $KAg_2Mn_2Cl_7$ is higher than 89 K (180 K measured in experiment) in $K_3Mn_2Cl_7$ (*37*).

Previously, the trilinear coupling interaction $Q_{(\Gamma_3^-)}Q_{(X_2^+)}Q_{(X_3^-)}$ was predicted to produce robust ME coupling, in which the wFM can be switched if the polarization and X_3^- tilt mode can be switched simultaneously (*27*). This ME mechanism largely relies on the switching path, in which the change in the direction of the polarization must induce a change of the X_3^- tilt mode; however, the path cannot be guaranteed. Here, we find that the trilinear coupling interaction $Q_{(\Gamma_3^-)}Q_{(X_2^+)}Q_{(X_1^-)}$ underlying the out-of-plane polarization can be exploited to realize strong ME coupling, in which the X_2^+ and X_1^- modes control the direction of the wFM through a Dzyaloshinskii-Moriya (DM) interaction: $E_{DML} = \boldsymbol{D} \cdot (\boldsymbol{L} \times \boldsymbol{M})$, where $\boldsymbol{D}$ is the DM vector, $\boldsymbol{L} = \boldsymbol{S}_1 - \boldsymbol{S}_2$ is the AFM vector, and $\boldsymbol{M} = \boldsymbol{S}_1 + \boldsymbol{S}_2$ is the wFM vector for neighboring spins $\boldsymbol{S}$. X_2^+ and X_1^- will lead to an effective $\boldsymbol{D}$ vector along the $[001]_{pt}$ direction (hereafter specified as $\boldsymbol{D}_{[001]_{pt}}$) given by $\boldsymbol{D} \sim \boldsymbol{r}_1 \times \boldsymbol{r}_2$, where $\boldsymbol{r}_i$ (i = 1, 2) is the unit vector pointing along the $\boldsymbol{S}_i$-O bond direction (*45*); hence, $[001]_{pt}$ is determined by $\boldsymbol{r}_1 \times \boldsymbol{r}_2$. Switching of the wFM direction then requires a reversal in the sense of either X_2^+ or X_1^-, which can be realized by switching the Γ_3^- mode, i.e., the direction of the out-of-plane polarization that can be coupled to an out-of-plane electric field in a standard FET geometry. Our climbing nudged elastic band (*46*) calculation shows an energy barrier of 82 meV/f.u. for reversing the monodomain state (fig. S8), which is comparable to other RP oxides such as $Sr_3Sn_2O_7$ and $Sr_3Zr_2O_7$ (*14*, *45*, *47*, *48*) and supports switchablilty of the out-of-plane polarization in the *Pc* phase.

There are only four Γ_3^- switching scenarios. Two cases are related to switching of the Γ_3^- mode and X_2^+ mode together [(Γ_3^-, M_5^+, X_2^+, X_3^-) and (Γ_3^-, Γ_5^-, M_5^-, X_2^+)]; the other two are related to switching of the Γ_3^- mode and X_1^- mode simultaneously [(Γ_3^-, Γ_5^-, M_5^-, X_1^-, X_3^-) and (Γ_3^-,M_5^+, X_1^-)]. Thus, one of either the X_2^+ or X_1^- mode must reverse upon switching the Γ_3^- mode. As can be seen in Fig. 1, the X_2^+ and X_1^- modes are in-phase and out-of-phase rotations, respectively, and will result in different alignments of the layer-resolved contributions to the wFM (Fig. 2C). For example, if X_2^+ is reversed 180° from a clockwise sense (as depicted) to counterclockwise, then the symmetry requires that wFMs in layers 1 to 4 will change so that the spin moments in layer 1 → layer 4, layer 2 → layer 3, layer 3 → layer 2, and layer 4 → layer 1 change, although the total wFM direction is unchanged. This switching of the wFM spin directions is also found in our DFT calculations including spin-orbital coupling (SOC).

As an alternative, we propose a ME coupling form for the RP compounds that does not depend on the switching path, where the polarization switching will uniquely change the wFM direction if the magnetic anisotropy (MA) is in plane. An in-plane MA can be obtained through a spin-flop mechanism (*49*). The magnetic field (H) to induce such a spin flop is proportional to $2S\sqrt{JK}$ (*45*), where S is the magnetic moment for each Mn, J is the maximum spin exchange parameter (i.e., J_2), and K is the single-ion anisotropy parameter. The computed H = 3.7 T in $KAg_2Mn_2Cl_7$, which is consistent with our Monte Carlo (MC) simulation with an applied magnetic field. Furthermore, the out-of-plane MA may be overcome by temperature effects, as an in-plane MA is observed near the Néel temperature in our MC simulations (fig. S10). The MA can also be changed in other ways such as a controllable

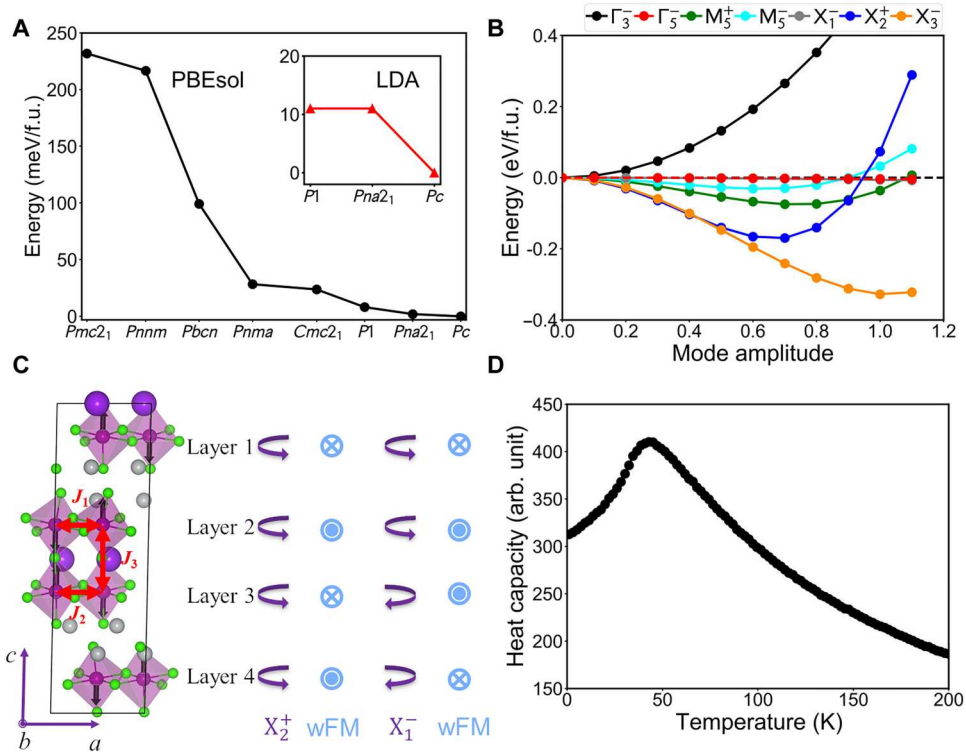

Fig. 2. Energetics and magnetism in $KAg_2Mn_2Cl_7$. (**A**) Energies for several symmetries of $KAg_2Mn_2Cl_7$. (**B**) Energy as a function of mode amplitude for each mode in the *Pc* structure. The mode amplitude is scaled by the original mode amplitude in Å in the *Pc* structure. (**C**) *Pc* structure with G-type magnetic structure along the pseudotetragonal *z* direction. The spin exchange interaction parameters are shown with the red arrows. X_2^+ and X_1^- rotations are represented by the arcs rotating about the pseudotetragonal *z* direction. The directions of the layer-resolved wFM components are indicated by the filled and crossed circles pointing to the *b* axis. (**D**) The simulated heat capacity as a function of temperature.

lateral MA in a heterostructure by atomic-scale design of the oxygen octahedral rotation (*50*, *51*).

To further elucidate the generality of the Γ_3^- mode for producing out-of-plane polarizations in the $n = 2$ RP family, we investigate *A*-site ordered $AA'_2B_2S_7$ sulfides. $ATb_2Fe_2O_7$ (A = Sr, Ca) were reported in a previous study combining experiment measurements and DFT calculations (*33*), in which the ground-state structures of $SrTb_2Fe_2O_7$ ($\tau = 0.944$) and $CaTb_2Fe_2O_7$ ($\tau = 0.941$) are $P4_2/mnm$ and $Cmc2_1$, respectively. We find, however, that the ground-state structure of $CaTb_2Fe_2O_7$ is *Pnma* by carrying out the DFT calculations at 0 K with the parameters provided in the previous study (*33*). This is consistent with another study on $Li_2SrNb_2O_7$ ($\tau = 0.964$) (*52*), in which the ground-state structure is *Pnma* and the $Cmc2_1$ phase is stabilized at finite temperatures owing to vibrational entropy. Therefore, the observed room-temperature $Cmc2_1$ phase in (Ca, Sr)$Tb_2Fe_2O_7$ occurs for the same reason as finding a $Cmc2_1$ phase at the high temperature in Li_2SrNbO_7. We hypothesize that the ground-state $n = 2$ RP phases are more complex than expected and the prior heuristic of lowering the tolerance factor may not lead to a polar ground state with $Cmc2_1$ symmetry.

With the low tolerance factor sulfide $SrTb_2Fe_2S_7$ ($\tau = 0.941$), we compare the energetics of common polymorphs identified from previous studies and find that the centrosymmetric $P4_2/mnm$ phase has the lowest energy (Fig. 3A). Our phonon calculations, however, reveal that the $P4_2/mnm$ phase is dynamically unstable (Fig. 3C), and the most unstable modes occur at the (0.5, 0.5, 0) and (0.5, 0.5, 0.5) k points in the Brillouin zone. Upon condensing different permutations of multiple modes from the same and different wave vectors (table S5), we find that the polar $I4_1cd$ structure is lowest in energy and comprises four main distortion modes (Fig. 4). The four phonon modes include one out-of-plane polar mode Γ_3^-, two AFE modes N_1^- and N_2^+, and one tilt mode X_3^-. The polar mode is distinct from that found in materials comprising second-order Jahn-Teller ions. Here, the X_3^- mode is different from the tilt mode in $Cmc2_1$ phase (one in-plane polar mode Γ_5^-, two rotational modes X_2^+, and X_3^- that results in *Cmcm* symmetry), where the rotational axes between the two double-perovskite layers are perpendicular to each other resulting in $P4_2/mnm$ symmetry and the DM vectors are along their rotational axes and normal to each other. In our magnetic calculations, we find a G-type magnetic structure with an in-plane MA. Then, the direction of wFM in a double-perovskite layer will be along the out-of-plane direction (see Fig. 5A).

Upon analyzing the symmetry relationships among the modes with $I4/mmm$ as reference, we obtain two important trilinear coupling interactions: $X_3^-N_1^-N_2^+$ and $\Gamma_3^-N_1^-N_2^+$. Thus, the direction of the X_3^- mode can be tuned by switching the Γ_3^- mode, in which the reversal of Γ_3^- will lead to a change of the sign of $N_1^-N_2^+$ that will result in a switching of X_3^- as to keep $X_3^-N_1^-N_2^+$ and $\Gamma_3^-N_1^-N_2^+$ invariant. Because the X_3^- mode can control the wFM and the existence of the trilinear coupling interactions as mentioned above, the switching of the polarization will unambiguously change the wFM, which does not depend on the switching path. Although the wFM

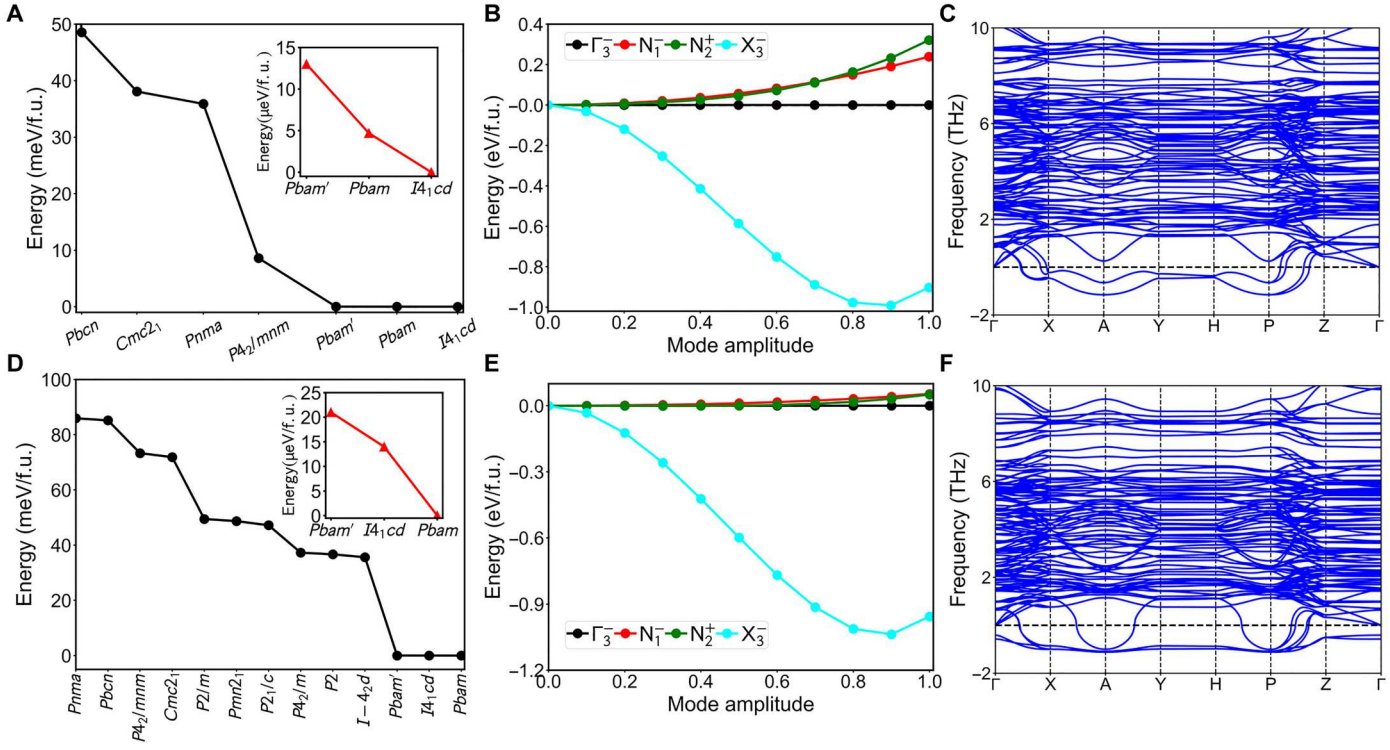

Fig. 3. Energetics and dynamical stability of $SrTb_2Fe_2S_7$ and $BaLa_2In_2S_7$. (**A**) Energies for several symmetries of $SrTb_2Fe_2S_7$. (**B**) Energy versus mode amplitude in $SrTb_2Fe_2S_7$ with the mode amplitude given relative to the mode amplitude found in the equilibrium $I4_1cd$ phase. (**C**) Phonon spectrum of $P4_2/mnm$ $SrTb_2Fe_2S_7$. (**D**) Energies for several symmetries of $BaLa_2In_2S_7$. (**E**) Energy versus mode amplitude in $BaLa_2In_2S_7$ with the mode amplitude given relative to the mode amplitude found in the equilibrium $I4_1cd$ phase. (**F**) Phonon spectrum of $P4_2/mnm$ $BaLa_2In_2S_7$.

components align in an antiparallel manner, so that there is no net magnetism, their directions in each perovskite layer can be switched upon changing the X_3^- mode as in $KAg_2Mn_2Cl_7$. Alloying may provide a route to canted magnetism. Furthermore, our ME coupling can be applied in devices on the basis of topological defects formed at the domain walls, in which a Z_8/Z_4 vortex or antivortex is formed in a $P4_2/mnm$ phase in $(Nd, Tb, Sr)_3Fe_2O_7$ (*44*) and $SrCa_2Ti_2O_7$ (*31*). The Z_8/Z_4 vortex and antivortex form because of the X_3^- mode in the $P4_2/mnm$ phase. If the X_3^- mode is further coupled to the polar Γ_3^- mode, such as in the $I4_1cd$ phase, then the robust ME coupling in Fig. 5A may be realized at a Z_8 vortex (see Fig. 5B and fig. S11). The in-plane and out-of-plane spin exchange parameters are computed and the Néel temperature is predicted to be 800 K from our MC simulations (Fig. 5C). The $I4_1cd$ structure is always more stable than the competitive *Pbam* phase at finite temperature and we calculate its FE Curie temperature as 455 K. Therefore, we predict $SrTb_2Fe_2S_7$ is a room-temperature multiferroic with strong ME coupling.

DISCUSSION

Multiferroics have been intensively studied since the discovery of room-temperature multiferroic $BiFeO_3$ (*53*) and type II multiferroic $TbMnO_3$ (*54*). Nowadays, electric-field control of magnetism has become a key to realize ultralow-power logic memory devices in recently developed device architectures (*55*, *56*). One priority for the scientific community is to broaden the set of materials that exhibit multiferroic and ME behavior at room temperature. From a technology perspective, finding robustly coupled FE and magnetic order parameters at the 10-nm length scale and at room temperature that are CMOS compatible for integration is critical. Therefore, combining persistent out-of-plane polarization and magnetism to realize strong ME coupling is of both scientific and technological importance. It is rarely reported with an unambiguously determined ME coupling mechanism (*24*, *57*). $SrTb_2Fe_2S_7$ may be such a promising room-temperature multiferroic with strong ME coupling satisfying the above requirements. Moreover, the most recent study showed that Hf-based FEs exhibit both ferroelectricity in ultrathin films (e.g., ~2 nm) and a large dielectric constant (~34), which has been intensively investigated and showed a very small equivalent oxide thickness (EOT) of 6.5 Å in a HfO_2-ZrO_2 superlattice (*11*). To obtain the small EOT, the small thickness and large static dielectric constant are required. In our studied compounds, $KAg_2Mn_2Cl_7$ may have a persistent polarization at a thickness of 2.3 nm with a dielectric constant of 3.6. $SrTb_2Fe_2S_7$ may have a persistent polarization at a thickness of 4.5 nm with a dielectric constant of 99 that is much larger than those of HfO_2 and ZrO_2 (*58*). Therefore, $SrTb_2Fe_2S_7$ may also be a potential candidate for designing advanced transistors with small EOT.

We also investigated other nonmagnetic *A*-site ordered RP sulfides and our results show that lower tolerance factors (e.g., $\tau <$ 0.944) may lead to an unstable $P4_2/mnm$ structure and then a lower-energy polar phase with out-of-plane polarization (fig. S13 and table S7). With this principle, we can select $BaLa_2In_2S_7$. We find that it adopts a competitive polar phase with $I4_1cd$ symmetry,

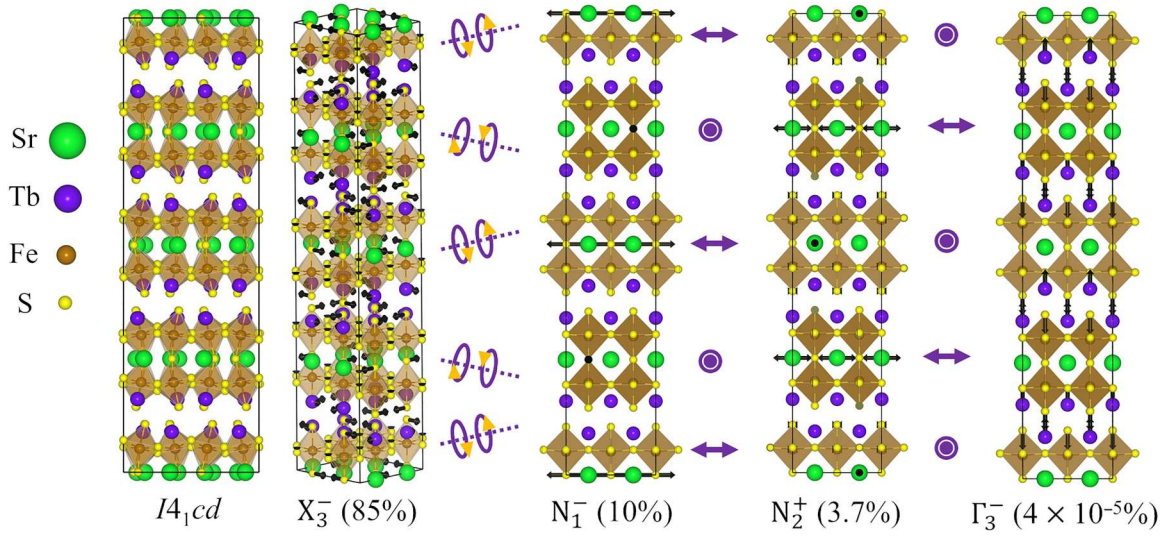

Fig. 4. Atomic structure of $SrTb_2Fe_2S_7$. Ground-state structure of $I4_1cd$ $SrTb_2Fe_2S_7$ and the main distortion modes obtained by a phonon decomposition with respect to $I4/mmm$. The schematic displacement patterns (e.g., purple arrows and circles) for the X_3^-, N_1^- and N_2^+ modes are shown for better visualization. Mode contributions (in percent) are given in descending order (as specified in parentheses).

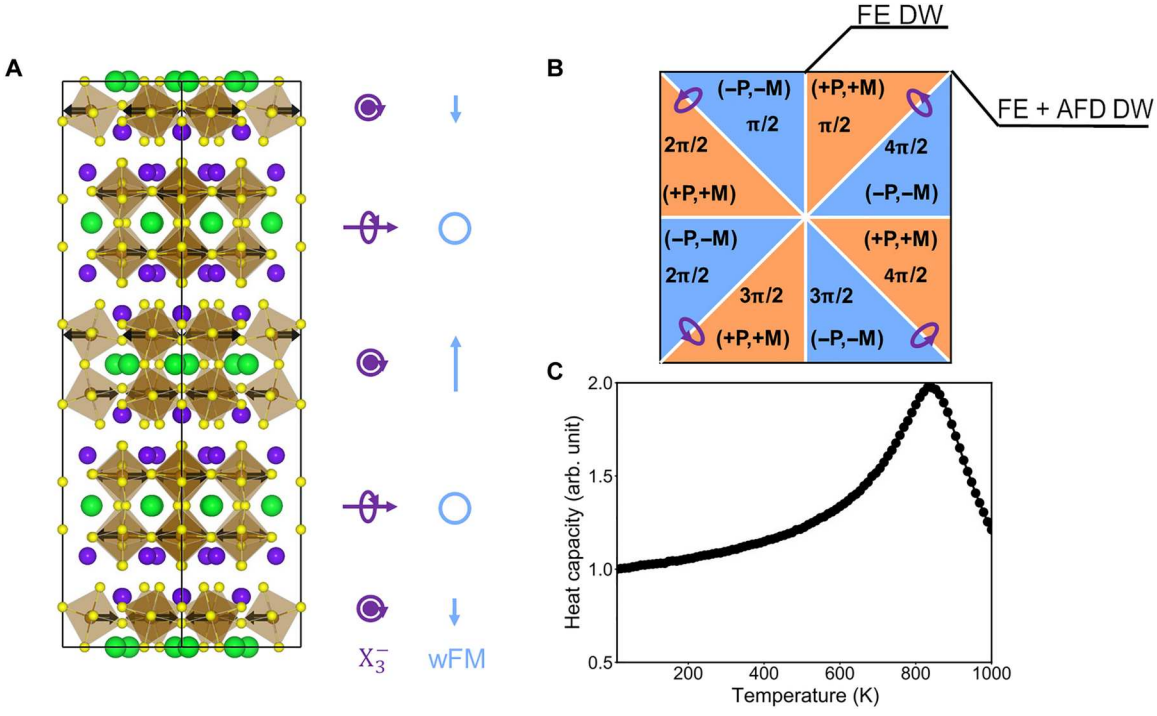

Fig. 5. Distortions and magnetism in $SrTb_2Fe_2S_7$. (**A**) The $I4_1cd$ $SrTb_2Fe_2S_7$ structure with G-type magnetic structure along the in-plane diagonal direction (i.e., *ab* direction). X_3^- rotations are represented by the arcs rotating around the in-plane directions. Black arrows within the octahedra indicate local spin vectors. The purple arrows on the right of the structure indicate the directions of the wFM in each perovskite bilayer. The wFM vectors along the *c* axis in the different double-perovskite layers will be opposite and cancel so that there is no net wFM. The blue circles indicate that there will be no wFM in the layers. (**B**) Schematic illustration of the switching paths between +**P** and −**P** states at a Z_8 vortex in $SrTb_2Fe_2S_7$. The degrees indicate the rotational angles of the X_3^- mode. The Z_8 vortex is formed by the X_3^- and Γ_3^- modes. The **P** and **M** represent the polarization and wFM, respectively. The white lines are the FE domain wall (FE DW) and FE DW plus antiferrodistortive domain wall (FE + AFD DW). The blue and orange areas represent the (−**P**, −**M**) and (+**P**, +**M**) states, respectively. (**C**) The simulated temperature-dependent heat capacity of $SrTb_2Fe_2S_7$.

whose ground-state structure is an AFE *Pbam* structure. The electric polarizations in $SrTb_2Fe_2S_7$ and $BaLa_2In_2S_7$ are due to hybrid improper ferroelectricity and 0.012 and 0.027 μC cm^{-2}, respectively (Fig. 3 and fig. S14). A large portion of their polarizations arise from the positive LO modes (see fig. S15), which indicates that the polarization in $SrTb_2Fe_2S_7$ and $BaLa_2In_2S_7$ should also persist under open-circuit boundary conditions. Our results also indicate that the ground-state $I4_1cd$ structure may be obtained in a RP sulfide compound with $0.938 < \tau < 0.944$. The larger τ may lead to a $P4_2/mnm$ ground-state structure and smaller τ may result in an AFE *Pbam* structure. This rule is also consistent with that found in RP oxides, where the ground-state phase has *Pnma* symmetry when τ is too small.

Regarding our studied materials, we expect that similar experimental measurements are applicable to reveal their FE and ME features. We notice that the melting points of halides are lower than oxides, implying that it is likely easier to obtain large single crystals, which are more suitable for precise physical property measurements especially for studying the polarization anisotropy, which is crucial for studying the persistent polarization, for example, in $KAg_2Mn_2Cl_7$. It adopts a polar monoclinic *Pc* structure with both in-plane and out-of-plane polarization. Large single crystals would enable the deconvolution of these contributions, allowing for a direct measurement of polarization and its switching along different directions. There are other possible experiments to further elucidate the FE and ME behaviors in our proposed materials. For example, in situ synchrotron x-ray diffraction experiment under applied electric fields can help understand the FE switching mechanism, as already demonstrated in HIF oxide $Ca_{2.15}Sr_{0.85}Ti_2O_7$ (*59*). Variable-temperature high-resolution neutron diffraction is also helpful in observing the coupling effect between electric polarization and magnetic order (*60*). Notably, this method has been particularly successful in our recent study on the first halide HIF ME $K_3Mn_2Cl_7$ (*37*), from which we observed that the long-range magnetic order induces a clear reduction in electric polarization. Beyond these reported experimental approaches, we believe that polarized-neutron diffraction experiments under electric fields would also be useful in directly observing electric field–induced modulation (or even switching) of the ferromagnetic component in our proposed materials.

In summary, we unveiled an out-of-plane LO mode in the $n = 2$ RP sulfides and halides that leads to persistent polarizations and makes them hybrid improper FEs. On the basis of a crystallographic tolerance factor, this out-of-plane polar mode can be predicted and more FE/multiferroic materials with out-of-plane hybrid improper ferroelectricity can be found when $0.938 < \tau < 0.944$. Our results show that $KAg_2Mn_2Cl_7$ and $SrTb_2Fe_2S_7$ are within this tolerance regime and are multiferroics. The Néel temperature for $SrTb_2Fe_2S_7$ is well above the room temperature. Both multiferroics exhibit strong ME couplings because of the existence of an out-of-plane polarization, in which switching of the polarization unambiguously induces a change in the wFM in the double-perovskite layers. We believe that our proposed polar mode is ubiquitous in the $n = 2$ RP family, for example, it may also be obtained in $n = 2$ RP oxides by an electric field when an antipolar *Pnma* polymorph is the ground-state structure ($\tau = 0.964$) (*32*), which provides a way to find promising FEs and multiferroics for device integration.

MATERIALS AND METHODS

Our total energy calculations are based on DFT within the generalized gradient approximation using the revised PBEsol (*61*) implemented in the Vienna Ab Initio Simulation Package (*62*, *63*). We use a 550-eV plane wave cutoff energy for all calculations and the projector augmented wave method (*64*, *65*). We use Gaussian smearing (0.10 eV width) for the Brillouin-zone integrations and a sufficiently dense *k*-point mesh. The pseudopotentials for the *A*- and *B*-site ions are chosen to treat the *s* or *p* core electrons as the valence electrons if available. The electric polarization is computed with the Berry phase method (*66*, *67*). The DFT plus Hubbard *U* method (*68*) is used with the Hubbard *U* and the exchange parameter *J* set to 6 eV and 1 eV for Mn, respectively, which reproduces the ground-state $Cmc2_1$ structure and the experimentally G-type antiferromagnetic structure in $K_3Mn_2Cl_7$ (*37*). The magnitude of wFM can be changed from 1×10^{-4} μB/Mn to 1×10^{-3} μB/Mn when changing the Hund's parameter *J* from 1 to 2 eV. Our DFT + *U* calculations also showed good agreement with the experiment structural parameters (lattices and atomic coordinates) and Néel temperature for $K_3Mn_2Cl_7$ (*37*). *U* and *J* are set to 5.5 and 1 eV for Fe, respectively, which reproduces the experimentally G-type antiferromagnetic structure in $SrTb_2Fe_2O_7$ (*33*). SOC is included for the MA studies.

To compute the symmetric spin exchange parameters, we use a four-state mapping method (*69*, *70*). We calculate the effective symmetric spin exchange parameters, which are obtained by setting $|\boldsymbol{S}_i|=1$, namely, $J_{ij} = J_{ij}^{\text{eff}} S_i S_j$ for a spin dimer *ij*. Our parallel tempering MC (PTMC) simulations are based on an exchange MC method (*39*, *71*), which can simulate the classical Heisenberg spin system with a Hamiltonian $E = E_0 + \sum_{i,j} J_{ij} \boldsymbol{S}_i \cdot \boldsymbol{S}_j$, where J_{ij} is the symmetric spin exchange parameter. To obtain the plot of the specific heat (C) versus temperature (T), we calculate the specific heat $C \sim (\langle E^2 \rangle - \langle E \rangle^2)/T^2$ after the system reaches equilibrium at a given temperature T in the simulation. Then, we obtain the critical temperature by locating the maximum in the $C(T)$ plot. In our PTMC simulations of the effective Hamiltonian, a $6 \times 6 \times 3$ supercell of the 48-atom unit cell is adopted for $KAg_2Mn_2Cl_7$ and a $6 \times 6 \times 3$ supercell of the 384-atom unit cell is adopted for $SrTb_2Fe_2S_7$, which we confirmed are converged. The number of replicas is set to 96.

For our phonon calculations, we use the finite displacements method (*72*). The symmetry-adapted mode distortion vectors of the polar phase are obtained by performing a mode decomposition with respect to *I*4/*mmm* using the ISODISTORT software (*73*).

To relax the mode amplitudes at each *u* (the amplitude of the fixed mode Γ_3^- or Γ_5^-), we minimize the Landau phenomenological expansion obtained using group theory by directly carrying out the DFT calculations rather than fitting the coefficients in the expansion (*48*). Here, the normalized distortion modes (with the amplitude of each mode vector normalized to 1 Å) in the *Pc* phase (some of them are shown in Fig. 1) are constrained, that is, the order parameter direction is fixed; however, the internal atomic positions are allowed to vary according to the directions of the phonon distortions considered (the magnitude is relaxed in the optimization) and the lattice constant is also optimized. This allows us to obtain the total energies and dielectric constants efficiently and accurately as described in fig. S4.

To implement this constraint in our DFT calculations, we project the forces on the atoms in the DFT calculations onto the

normalized distortion modes except for the fixed mode (i.e., Γ_3^- or Γ_5^-) so that the order parameter direction is fixed, but the magnitude of the mode is relaxed in the optimization. Then, the amplitudes of phonon modes in the *Pc* phase will change for different u, but the modes vectors will all be the same as those at $u = 1$(i.e., the ground state) (*48*).

The tolerance factor is obtained by using $\tau_i = \frac{r_A + r_X}{\sqrt{2}(r_B + r_X)}$, where r_A, r_B, and r_X are the radii of the A, B cations, and anion, respectively. The averaged $r_{A-X} = r_A + r_X$ is computed by considering the nearest-neighboring oxygen atoms around the A atom for all A atoms. The averaged r_{B-X} is computed in the same way as r_{A-X}. Here, we consider 12-coordination for A, 9-coordination for A', and 6-coordination for B. The τ is computed in *Pc* phase for $KAg_2Mn_2Cl_7$, in *Pnma* for $CaTb_2Fe_2O_7$ and $SrLi_2NbO_7$, and in $P4_2/mnm$ for $SrTb_2Fe_2O_7$, $SrTb_2Fe_2S_7$ and $BaLa_2In_2S_7$ (table S7).

Supplementary Materials

This PDF file includes:

Supplementary Text
Figs. S1 to S15
Tables S1 to S9
References

REFERENCES AND NOTES

1. L. W. Martin, A. M. Rappe, Thin-film ferroelectric materials and their applications. *Nat. Rev. Mater.* **2**, 16087 (2017).
2. J. F. Scott, C. A. Paz De Araujo, Ferroelectric memories. *Science* **246**, 1400–1405 (1989).
3. K. Chang, J. Liu, H. Lin, N. Wang, K. Zhao, A. Zhang, F. Jin, Y. Zhong, X. Hu, W. Duan, Q. Zhang, L. Fu, Q. K. Xue, X. Chen, S. H. Ji, Discovery of robust in-plane ferroelectricity in atomic-thick SnTe. *Science* **353**, 274–278 (2016).
4. C. H. Ahn, K. M. Rabe, J. M. Triscone, Ferroelectricity at the nanoscale: Local polarization in oxide thin films and heterostructures. *Science* **303**, 488–491 (2004).
5. A. Fernandez, M. Acharya, H. G. Lee, J. Schimpf, Y. Jiang, D. Lou, Z. Tian, L. W. Martin, Thin-film ferroelectrics. *Adv. Mater.* **34**, e2108841 (2022).
6. Y. Wei, P. Nukala, M. Salverda, S. Matzen, H. J. Zhao, J. Momand, A. S. Everhardt, G. Agnus, G. R. Blake, P. Lecoeur, B. J. Kooi, J. Íñiguez, B. Dkhil, B. Noheda, A rhombohedral ferroelectric phase in epitaxially strained $Hf_{0.5}Zr_{0.5}O_2$ thin films. *Nat. Mater.* **17**, 1095–1100 (2018).
7. H. J. Lee, M. Lee, K. Lee, J. Jo, H. Yang, Y. Kim, S. C. Chae, U. Waghmare, J. H. Lee, Scale-free ferroelectricity induced by flat phonon bands in HfO_2. *Science* **369**, 1343–1347 (2020).
8. X. Xu, F. T. Huang, Y. Qi, S. Singh, K. M. Rabe, D. Obeysekera, J. Yang, M. W. Chu, S. W. Cheong, Kinetically stabilized ferroelectricity in bulk single-crystalline HfO_2:Y. *Nat. Mater.* **20**, 826–832 (2021).
9. Y. Yun, P. Buragohain, M. Li, Z. Ahmadi, Y. Zhang, X. Li, H. Wang, J. Li, P. Lu, L. Tao, H. Wang, J. E. Shield, E. Y. Tsymbal, A. Gruverman, X. Xu, Intrinsic ferroelectricity in Y-doped HfO_2 thin films. *Nat. Mater.* **21**, 903–909 (2022).
10. U. Schroeder, M. H. Park, T. Mikolajick, C. S. Hwang, The fundamentals and applications of ferroelectric HfO_2. *Nat. Rev. Mater.* **7**, 653–669 (2022).
11. S. S. Cheema, N. Shanker, L. C. Wang, C. H. Hsu, S. L. Hsu, Y. H. Liao, M. San Jose, J. Gomez, W. Chakraborty, W. Li, J. H. Bae, S. K. Volkman, D. Kwon, Y. Rho, G. Pinelli, R. Rastogi, D. Pipitone, C. Stull, M. Cook, B. Tyrrell, V. A. Stoica, Z. Zhang, J. W. Freeland, C. J. Tassone, A. Mehta, G. Saheli, D. Thompson, D. I. Suh, W. T. Koo, K. J. Nam, D. J. Jung, W. Bin Song, C. H. Lin, S. Nam, J. Heo, N. Parihar, C. P. Grigoropoulos, P. Shafer, P. Fay, R. Ramesh, S. Mahapatra, J. Ciston, S. Datta, M. Mohamed, C. Hu, S. Salahuddin, Ultrathin ferroic HfO_2–ZrO_2 superlattice gate stack for advanced transistors. *Nature* **604**, 65–71 (2022).
12. N. A. Benedek, J. M. Rondinelli, H. Djani, P. Ghosez, P. Lightfoot, Understanding ferroelectricity in layered perovskites: New ideas and insights from theory and experiments. *Dalt. Trans.* **44**, 10543–10558 (2015).
13. R. Ramesh, D. G. Schlom, Orienting ferroelectric films. *Science* **296**, 1975–1976 (2002).
14. A. T. Mulder, N. A. Benedek, J. M. Rondinelli, C. J. Fennie, Turning ABO_3 antiferroelectrics into ferroelectrics: Design rules for practical rotation-driven ferroelectricity in double perovskites and $A_3B_2O_7$ ruddlesden-popper compounds. *Adv. Funct. Mater.* **23**, 4810–4820 (2013).
15. S. Benomar, E. Bousquet, H. Djani, Multianion induced out-of-plane proper polarization in oxyfluoride aurivillius $Bi_2TiO_4F_2$. *J. Phys. Chem. Solids.* **167**, 110720 (2022).
16. T. Birol, N. A. Benedek, C. J. Fennie, Interface control of emergent ferroic order in Ruddlesden-Popper $Sr_{n+1}Ti_nO_{3n+1}$. *Phys. Rev. Lett.* **107**, 257602 (2011).
17. J. Junquera, P. Ghosez, Critical thickness for ferroelectricity in perovskite ultrathin films. *Nature* **422**, 506–509 (2003).
18. D. D. Fong, G. B. Stephenson, S. K. Streiffer, J. A. Eastman, O. Aucielo, P. H. Fuoss, C. Thompson, Ferroelectricity in ultrathin perovskite films. *Science* **304**, 1650–1653 (2004).
19. K. F. Garrity, K. M. Rabe, D. Vanderbilt, Hyperferroelectrics: Proper ferroelectrics with persistent polarization. *Phys. Rev. Lett.* **112**, 127601 (2014).
20. N. Sai, C. J. Fennie, A. A. Demkov, Absence of critical thickness in an ultrathin improper ferroelectric film. *Phys. Rev. Lett.* **102**, 107601 (2009).
21. R. Adhikari, H. Fu, Hyperferroelectricity in ZnO: Evidence from analytic formulation and numerical calculations. *Phys. Rev. B* **99**, 104101 (2019).
22. P. Li, X. Ren, G. C. Guo, L. He, The origin of hyperferroelectricity in $LiBO_3$ (B = V, Nb, Ta, Os). *Sci. Rep.* **6**, 34085 (2016).
23. G. Roma, A. Marronnier, J. Even, From latent ferroelectricity to hyperferroelectricity in alkali lead halide perovskites. *Phys. Rev. Mater.* **4**, 092402(R) (2020).
24. M. Markov, L. Alaerts, H. P. Coutada Miranda, G. Petretto, W. Chen, J. George, E. Bousquet, P. Ghosez, G. M. Rignanese, G. Hautier, Ferroelectricity and multiferroicity in anti–Ruddlesden–Popper structures. *Proc. Natl. Acad. Sci. U.S.A.* **118**, e2026020118 (2021).
25. E. Bousquet, M. Dawber, N. Stucki, C. Lichtensteiger, P. Hermet, S. Gariglio, J. M. Triscone, P. Ghosez, Improper ferroelectricity in perovskite oxide artificial superlattices. *Nature* **452**, 732–736 (2008).
26. J. M. Rondinelli, C. J. Fennie, M. Rondinelli, C. J. Fennie, Octahedral rotation-induced ferroelectricity in cation ordered perovskites. *Adv. Mater.* **24**, 1961–1968 (2012).
27. N. A. Benedek, C. J. Fennie, Hybrid improper ferroelectricity: A mechanism for controllable polarization-magnetization coupling. *Phys. Rev. Lett.* **106**, 107204 (2011).
28. B. B. Van Aken, T. T. M. Palstra, A. Filippetti, N. A. Spaldin, The origin of ferroelectricity in magnetoelectric $YMnO_3$. *Nat. Mater.* **3**, 164–170 (2004).
29. N. A. Benedek, M. A. Hayward, Hybrid improper ferroelectricity: A theoretical, computational and synthetic perspective. *Annu. Rev. Mater. Res.* **52**, 331–355 (2022).
30. Y. S. Oh, X. Luo, F. T. Huang, Y. Wang, S. W. Cheong, Experimental demonstration of hybrid improper ferroelectricity and the presence of abundant charged walls in $(Ca,Sr)_3Ti_2O_7$ crystals. *Nat. Mater.* **14**, 407–413 (2015).
31. F.-T. Huang, B. Gao, J.-W. Kim, X. Luo, Y. Wang, M.-W. Chu, C.-K. Chang, H.-S. Sheu, S.-W. Cheong, Topological defects at octahedral tilting plethora in bi-layered perovskites. *npj Quantum Mater.* **1**, 16017 (2016).
32. Y. Mochizuki, T. Nagai, H. Shirakuni, A. Nakano, F. Oba, I. Terasaki, H. Taniguchi, Coexisting mechanisms for the ferroelectric phase transition in $Li_2SrNb_2O_7$. *Chem. Mater.* **33**, 1257–1264 (2021).
33. M. J. Pitcher, P. Mandal, M. S. Dyer, J. Alaria, P. Borisov, H. Niu, J. B. Claridge, M. J. Rosseinsky, Tilt engineering of spontaneous polarization and magnetization above 300 K in a bulk layered perovskite. *Science* **347**, 420–424 (2015).
34. M. Liu, Y. Zhang, L.-F. Lin, L. Lin, S. Yang, X. Li, Y. Wang, S. Li, Z. Yan, X. Wang, X.-G. Li, S. Dong, J.-M. Liu, Direct observation of ferroelectricity in $Ca_3Mn_2O_7$ and its prominent light absorption. *Appl. Phys. Lett.* **113**, 22902 (2018).
35. T. Zhu, A. S. Gibbs, N. A. Benedek, M. A. Hayward, Complex structural phase transitions of the hybrid improper polar Dion-Jacobson Oxides $RbNdM_2O_7$ and $CsNdM_2O_7$ (M = Nb, Ta). *Chem. Mater.* **32**, 4340–4346 (2020).
36. N. A. Benedek, Origin of ferroelectricity in a family of polar oxides: The Dion-Jacobson phases. *Inorg. Chem.* **53**, 3769–3777 (2014).
37. T. Zhu, X. Lu, T. Aoyama, K. Fujita, Y. Nambu, T. Saito, H. Takatsu, T. Kawasaki, T. Terauchi, S. Kurosawa, A. Yamaji, H.-B. Li, C. Tassel, K. Ohgushi, J. M. Rondinelli, H. Kageyama, Thermal magnetoelectrics in all inorganic quasi-two-dimensional halide perovskites. arXiv:2311.09324 (2023).
38. X. Z. Lu, X. G. Gong, H. J. Xiang, Polarization enhancement in perovskite superlattices by oxygen octahedral tilts. *Comput. Mater. Sci.* **91**, 310–314 (2014).
39. F. Lou, X. Y. Li, J. Y. Ji, H. Y. Yu, J. S. Feng, X. G. Gong, H. J. Xiang, PASP: Property analysis and simulation package for materials. *J. Chem. Phys.* **154**, 114103 (2021).
40. X. Q. Liu, J. W. Wu, X. X. Shi, H. J. Zhao, H. Y. Zhou, R. H. Qiu, W. Q. Zhang, X. M. Chen, Hybrid improper ferroelectricity in Ruddlesden-Popper $Ca_3(Ti,Mn)_2O_7$ ceramics. *Appl. Phys. Lett.* **106**, 202903 (2015).
41. A. B. Harris, Symmetry analysis for the Ruddlesden-Popper systems $Ca_3Mn_2O_7$ and $Ca_3Ti_2O_7$. *Phys. Rev. B.* **84**, 064116 (2011).
42. Q. Yang, J. Hu, Y.-W. Fang, Y. Jia, R. Yang, S. Deng, Y. Lu, O. Dieguez, L. Fan, D. Zheng, X. Zhang, Y. Dong, Z. Luo, Z. Wang, H. Wang, M. Sui, X. Xing, J. Chen, J. Tian, L. Zhang, Ferroelectricity in layered bismuth oxide down to 1 nanometer. *Science* **379**, 1218–1224 (2023).

43. S. Artyukhin, K. T. Delaney, N. A. Spaldin, M. Mostovoy, Landau theory of topological defects in multiferroic hexagonal manganites. *Nat. Mater.* **13**, 42–49 (2014).
44. F. T. Huang, Y. Li, F. Xue, J. W. Kim, L. Zhang, M. W. Chu, L. Q. Chen, S. W. Cheong, Evolution of topological defects at two sequential phase transitions of $Nd_2SrFe_2O_7$. *Phys. Rev. Res.* **3**, 023216 (2021).
45. X. Z. Lu, J. M. Rondinelli, Room temperature electric-field control of magnetism in layered oxides with cation order. *Adv. Funct. Mater.* **27**, 1604312 (2017).
46. G. Henkelman, B. P. Uberuaga, H. Jónsson, A climbing image nudged elastic band method for finding saddle points and minimum energy paths. *J. Chem. Phys.* **113**, 9901–9904 (2000).
47. S. Li, T. Birol, Suppressing the ferroelectric switching barrier in hybrid improper ferroelectrics. *npj Comput. Mater.* **6**, 168 (2020).
48. X. Z. Lu, J. M. Rondinelli, Epitaxial-strain-induced polar-to-nonpolar transitions in layered oxides. *Nat. Mater.* **15**, 951–955 (2016).
49. N. Abe, N. D. Khanh, T. Sasaki, T. Arima, Magnetic-field-induced spin flop transition and magnetoelectric effect in $Ca_2Fe_{2-x}Al_xO_5$. *Phys. Rev. B* **89**, 054437 (2014).
50. Z. Liao, M. Huijben, Z. Zhong, N. Gauquelin, S. Macke, R. J. Green, S. Van Aert, J. Verbeeck, G. Van Tendeloo, K. Held, G. A. Sawatzky, G. Koster, G. Rijnders, Controlled lateral anisotropy in correlated manganite heterostructures by interface-engineered oxygen octahedral coupling. *Nat. Mater.* **15**, 425–431 (2016).
51. D. Kan, R. Aso, R. Sato, M. Haruta, H. Kurata, Y. Shimakawa, Tuning magnetic anisotropy by interfacially engineering the oxygen coordination environment in a transition metal oxide. *Nat. Mater.* **15**, 432–437 (2016).
52. R. Uppuluri, H. Akamatsu, A. Sen Gupta, H. Wang, C. M. Brown, K. E. Agueda Lopez, N. Alem, V. Gopalan, T. E. Mallouk, Competing polar and antipolar structures in the Ruddlesden-Popper layered perovskite $Li_2SrNb_2O_7$. *Chem. Mater.* **31**, 4418–4425 (2019).
53. J. Wang, J. B. Neaton, H. Zheng, V. Nagarajan, S. B. Ogale, B. Liu, D. Viehland, V. Vaithyanathan, D. G. Schlom, U. V. Waghmare, N. A. Spaldin, K. M. Rabe, M. Wuttig, R. Ramesh, Epitaxial $BiFeO_3$ multiferroic thin film heterostructures. *Science* **299**, 1719–1722 (2003).
54. T. Kimura, T. Goto, H. Shintani, K. Ishizaka, T. Arima, Y. Tokura, Magnetic control of ferroelectric polarization. *Nature* **426**, 55–58 (2003).
55. N. A. Spaldin, R. Ramesh, Advances in magnetoelectric multiferroics. *Nat. Mater.* **18**, 203–212 (2019).
56. A. C. Garcia-Castro, Y. Ma, Z. Romestan, E. Bousquet, C. Cen, A. H. Romero, Engineering of ferroic orders in thin films by anionic substitution. *Adv. Funct. Mater.* **32**, 2107135 (2022).
57. H. Das, A. L. Wysocki, Y. Geng, W. Wu, C. J. Fennie, Bulk magnetoelectricity in the hexagonal manganites and ferrites. *Nat. Commun.* **5**, 2998 (2014).
58. K. Yim, Y. Yong, J. Lee, K. Lee, H. H. Nahm, J. Yoo, C. Lee, C. S. Hwang, S. Han, Novel high-K dielectrics for next-generation electronic devices screened by automated ab initio calculations. *NPG Asia Mater.* **7**, e190 (2015).
59. G. Clarke, C. Ablitt, J. Daniels, S. Checchia, M. S. Senn, In situ X-ray diffraction investigation of electric-field-induced switching in a hybrid improper ferroelectric. *J. Appl. Crystallogr.* **54**, 533–540 (2021).
60. T. Zhu, F. Orlandi, P. Manuel, A. S. Gibbs, W. Zhang, P. S. Halasyamani, M. A. Hayward, Directed synthesis of a hybrid improper magnetoelectric multiferroic material. *Nat. Commun.* **12**, 4945 (2021).
61. J. P. Perdew, A. Ruzsinszky, G. I. Csonka, O. A. Vydrov, G. E. Scuseria, L. A. Constantin, X. Zhou, K. Burke, Restoring the density-gradient expansion for exchange in solids and surfaces. *Phys. Rev. Lett.* **100**, 136406 (2008).
62. G. Kresse, J. Furthmüller, Efficiency of ab-initio total energy calculations for metals and semiconductors using a plane-wave basis set. *Comput. Mater. Sci.* **6**, 15–50 (1996).
63. G. Kresse, J. Furthmüller, Efficient iterative schemes for ab initio total-energy calculations using a plane-wave basis set. *Phys. Rev. B* **54**, 11169 (1996).
64. G. Kresse, D. Joubert, From ultrasoft pseudopotentials to the projector augmented-wave method. *Phys. Rev. B* **59**, 1758 (1999).
65. P. E. Blöchl, Projector augmented-wave method. *Phys. Rev. B* **50**, 17953 (1994).
66. R. Resta, Macroscopic polarization in crystalline dielectrics: The geometric phase approach. *Rev. Mod. Phys.* **66**, 899 (1994).
67. R. D. King-Smith, D. Vanderbilt, Theory of polarization of crystalline solids. *Phys. Rev. B* **47**, 1651 (1993).
68. A. I. Liechtenstein, V. I. Anisimov, J. Zaanen, Density-functional theory and strong interactions: Orbital ordering in Mott-Hubbard insulators. *Phys. Rev. B* **52**, R5467(R) (1995).
69. H. Xiang, C. Lee, H. J. Koo, X. Gong, M. H. Whangbo, Magnetic properties and energy-mapping analysis. *Dalt. Trans.* **42**, 823–853 (2013).
70. H. J. Xiang, E. J. Kan, S. H. Wei, M. H. Whangbo, X. G. Gong, Predicting the spin-lattice order of frustrated systems from first principles. *Phys. Rev. B* **84**, 224429 (2011).
71. K. Hukushima, K. Nemoto, Exchange monte carlo method and application to spin glass simulations. *J Phys. Soc Japan.* **65**, 1604–1608 (1996).
72. A. Togo, I. Tanaka, First principles phonon calculations in materials science. *Scr. Mater.* **108**, 1–5 (2015).
73. B. J. Campbell, H. T. Stokes, D. E. Tanner, D. M. Hatch, ISODISPLACE: A web-based tool for exploring structural distortions. *J. Appl. Crystallogr.* **39**, 607–614 (2006).
74. R. Zhang, B. M. Abbett, G. Read, F. Lang, T. Lancaster, T. T. Tran, P. S. Halasyamani, S. J. Blundell, N. A. Benedek, M. A. Hayward, $La_2SrCr_2O_7$: Controlling the tilting distortions of n = 2 Ruddlesden-Popper phases through a-site cation order. *Inorg. Chem.* **55**, 8951–8960 (2016).
75. D. Puggioni, G. Giovannetti, M. Capone, J. M. Rondinelli, Design of a Mott multiferroic from a nonmagnetic polar metal. *Phys. Rev. Lett.* **115**, 087202 (2015).
76. J. T. Heron, J. L. Bosse, Q. He, Y. Gao, M. Trassin, L. Ye, J. D. Clarkson, C. Wang, J. Liu, S. Salahuddin, D. C. Ralph, D. G. Schlom, J. Íñiguez, B. D. Huey, R. Ramesh, Deterministic switching of ferromagnetism at room temperature using an electric field. *Nature* **516**, 370–373 (2014).
77. E. A. Nowadnick, C. J. Fennie, Domains and ferroelectric switching pathways in $Ca_3Ti_2O_7$ from first principles. *Phys. Rev. B* **94**, 104105 (2016).
78. J. M. Munro, H. Akamatsu, H. Padmanabhan, V. S. Liu, Y. Shi, L. Q. Chen, B. K. Vanleeuwen, I. Dabo, V. Gopalan, Discovering minimum energy pathways via distortion symmetry groups. *Phys. Rev. B* **98**, 085107 (2018).
79. M. Iliev, H. Lee, V. Popov, Raman- and infrared-active phonons in hexagonal $YMnO_3$: Experiment and lattice-dynamical calculations. *Phys. Rev. B* **56**, 2488 (1997).

Acknowledgments

Funding: This work was supported by the National Science Foundation grants DMR-2104397 (X.-Z.L.) and ACI-1548562 (to J.M.R.) and SUPREME, one of seven centers in JUMP 2.0, a Semiconductor Research Corporation (SRC) program sponsored by DARPA (J.M.R.). Computations were performed at the Center for Nanoscale Materials, a U.S. Department of Energy, Office of Science, Office of Basic Energy Sciences, under contract no. DE-AC02-06CH11357 (X.-Z.L. and J.M.R.). This work was also supported by Japan Society for the Promotion of Science (JSPS) Grant-in-Aid for Specially Promoted Research "Hydrogen Ion Ceramics" grant JP22H04914 (to H.K. and T.Z.). Part of the calculations was performed on the high-performance computers, supported by the Big Data Computing Center of Southeast University. **Author contributions:** Conceptualization: X.-Z.L. and J.M.R. Investigation: X.-Z.L., H.-M.Z., Y.Z., and T.Z. Writing–original draft: X.-Z.L. and J.M.R. Writing–review and editing: X.-Z.L., J.M.R., T.Z., H.K., H.X., and S.D. Project administration: X.-Z.L. and J.M.R. Funding acquisition: J.M.R. and H.K. **Competing interests:** The authors declare that they have no competing interests. **Data and materials availability:** All data needed to evaluate the conclusions of this paper are present in the paper and the Supplemental Materials, including crystal information files for the simulated structures, which are at: https://doi.org/10.5061/dryad.59zw3r2dr.

Submitted 28 March 2023
Accepted 23 October 2023
Published 22 November 2023
10.1126/sciadv.adi0138